Probing *Clostridium difficile* infection in innovative human gut cellular models

Blessing O. Anonye[1], Jack Hassall[2], Jamie Patient[3], Usanee Detamornrat[3], Afnan M. Aladdad[3], Stephanie Schüller[4,5], Felicity R.A.J. Rose[3], Meera Unnikrishnan[1*]

[1]Microbiology and Infection Unit, Division of Biomedical Sciences, Warwick Medical School, University of Warwick, Coventry, United Kingdom

[2]Warwick Integrative Synthetic Biology Centre, School of Life Sciences, University of Warwick, Coventry, United Kingdom

[3]Division of Regenerative Medicine and Cellular Therapies, School of Pharmacy, Centre for Biomolecular Sciences, University of Nottingham, Nottingham, United Kingdom

[4]Norwich Medical School, University of East Anglia, Norwich, United Kingdom

[5]Gut Health and Food Safety Programme, Quadram Institute Bioscience, Norwich, United Kingdom

[*]**Correspondence:**
Meera Unnikrishnan, Division of Biomedical Sciences, Warwick Medical School, University of Warwick, Coventry, CV4 7AL, UK,
Email: m.unnikrishnan@warwick.ac.uk,

Keywords: *Clostridium difficile*, 3-D gut epithelium, gut infection model, colonization, *C. difficile*-commensal interactions, vertical diffusion chamber

Words: 6165

Abstract

Interactions of anaerobic gut bacteria, such as *Clostridium difficile,* with the intestinal mucosa have been poorly studied due to challenges in culturing anaerobes with the oxygen-requiring gut epithelium. Although gut colonization by *C. difficile* is a key determinant of disease outcome, precise mechanisms of mucosal attachment and spread remain unclear. Here, using human gut epithelial monolayers co-cultured within dual environment chambers, we demonstrate that *C. difficile* adhesion to gut epithelial cells is accompanied by a gradual increase in bacterial numbers. Prolonged infection causes redistribution of actin and loss of epithelial integrity, accompanied by production of *C. difficile* spores, toxins and bacterial filaments. This 2-D dual chamber system was used to examine *C. difficile* interactions with the commensal *Bacteroides dorei*, and interestingly, *C. difficile* growth is significantly reduced in presence of *B. dorei*. Furthermore, in novel multilayer and 3-D gut models containing a myofibroblast layer, *C. difficile* adheres more efficiently to epithelial cells, as compared to the 2-D model, leading to a quicker destruction of the epithelium. Our study describes new controlled environment human gut models that enable host-anaerobe and pathogen-commensal interaction studies *in vitro*.

INTRODUCTION

Clostridium difficile, an anaerobic spore-forming bacterium, is the main cause of infectious diarrhea in healthcare settings. A major risk factor for *C. difficile* infection (CDI) is antibiotic use, which results in the disruption of the intestinal microbiota, allowing *C. difficile* to colonize and proliferate (Adamu and Lawley, 2013; Fuentes et al., 2014). CDI is one of the most common healthcare-associated infections in the United States, with an estimated 453,000 cases of CDI and 29,000 deaths reported in 2011, and with the highest mortality rates among the elderly (Lessa et al., 2015). Although the number of cases in the UK are declining [13,000 cases in 2016-2017 (England, 2017)], an increasing incidence of CDI has been reported across Europe, Canada and Australia (Gravel et al., 2009; Davies et al., 2014; Collins et al., 2017).

CDI pathogenesis is complex and mediated by a number of bacterial virulence factors. *C. difficile* produces two main toxins, toxin A and toxin B (TcdA and TcdB), and some strains produce a binary toxin (CDT), all of which contribute to bacterial pathogenicity (Kuehne et al., 2014; Carter et al., 2015). Toxins A and B are known to disrupt the intestinal epithelial barrier function through inactivation of the Rho GTPases, which results in reorganization of the actin cytoskeleton and induction of the MAPK pathways, leading to a cytokine response (Bobo et al., 2013; Chen et al., 2015). The key role for these toxins during infection has been demonstrated in animal models using toxin mutants, which are unable to cause disease and death (Lyras et al., 2009; Kuehne et al., 2010; Kuehne et al., 2014; Carter et al., 2015). While toxins are major virulence factors, recent studies have highlighted the importance of several *C. difficile* surface proteins such as surface layer proteins (Calabi et al., 2002; Merrigan et al., 2013), adhesins (Hennequin et al., 2001; Barketi-Klai et al., 2011; Kovacs-Simon et al., 2014), cell wall proteins (Waligora et al., 2001), pili and flagella in CDI (Tasteyre et al., 2001; Batah et al., 2017; McKee et al., 2018). *C. difficile* is also known to produce spores that are resistant to antibiotics and disinfectants (Lawley et al., 2010; Vohra and Poxton, 2011). *C. difficile* spores mediate disease transmission and may serve as a reservoir within the host causing recurrence of infection (Deakin et al., 2012b).

Although animal models of CDI have been used to understand *C. difficile* pathogenesis and investigate the functions of several *C. difficile* factors (Chen et al., 2008; Kuehne et al., 2010; Deakin et al., 2012b; Darkoh et al., 2016), it is challenging to study host-bacterial interactions occurring at the gut mucosal interface *in vivo*. *In vitro* human cell culture models enable molecular and cellular studies on both the host and the pathogen, easier testing of multiple conditions and visualisation of infection dynamics. Infection of human intestinal epithelial cell (IEC) lines has been used to study *C. difficile* pathogenesis but these models have been limited to short time periods as *C. difficile* requires an anaerobic environment for optimal growth (Cerquetti et al., 2002; Janvilisri et al., 2010; Mora-Uribe et al., 2016). A dual environment system such as a vertical diffusion chamber (VDC), which permits growth of the bacteria and IECs in appropriate gaseous environments was used previously by Schüller and Phillips to demonstrate increased adherence of enterohaemorrhagic *Escherichia coli* (EHEC) to polarized IECs in microaerobic compared to aerobic conditions, accompanied by enhanced expression and translocation of EHEC type III secreted effector proteins (Schüller and Phillips, 2010). Similarly, an increase in *Campylobacter jejuni* invasion of IECs was observed under a microaerobic environment in the VDC (Mills et al., 2012). Recently, a VDC was employed to culture *C. difficile* with T84 cells where an anaerobic environment was shown to enhance *C. difficile*-induced cytokine production, compared to aerobic co-culture although this was only studied over a short time course (Jafari et al., 2016).

Models that replicate the physiology and local tissue environment found *in vivo* are ideal for investigating pathogen interactions in IECs. Three-dimensional (3-D) gut models support better epithelial cell growth and differentiation through proteins such as growth factors secreted by underlying cell layers (Morris et al., 2014; Kook et al., 2017). Scaffolds generated from natural or synthetic polymers such as matrigel, collagen and polyethylene terephthalate (PET) have been used to generate the extracellular matrix, which is a major tissue component, and supporting scaffolds can be designed to meet the cell type-specific needs. (Ravi et al., 2015; Kook et al., 2017). More recently, electrospinning has been employed to fabricate fibers from polymers creating a structure similar to the natural fibrous network of the extracellular matrix (ECM) (Morris et al., 2014; Kook et al., 2017). Electrospinning was used to create nanofiber and microfiber scaffolds for optimal 3-D *in vitro* culture of airway epithelial and fibroblast cells (Morris et al., 2014). Fibroblasts play an active role in producing ECM and producing chemokines in response to bacterial infection (Smith et al., 1997).

Three-dimensional gut models have been employed to understand key bacterial and host pathways in a range of pathogens including *C. difficile* (Kasendra et al., 2014; Leslie et al., 2015), *Salmonella* (Barrila et al., 2017), *Cryptosporidium parvum* (DeCicco RePass et al., 2017) and Coxsackievirus B (Drummond et al., 2016). In human intestinal organoids infected with *C. difficile,* bacteria were reported to be viable for up to 12h (Leslie et al., 2015), while a 3-D model using Caco-2 cells grown as cysts in a matrigel monitored the adhesion and translocation of *C. difficile* for 1h (Kasendra et al., 2014). While both studies investigated the role of *C. difficile* toxins in these models, neither was able to follow the infection for a longer period of time due to the lack of an optimal environment for bacterial growth.

In this study, we have determined the infection dynamics of *C. difficile* over an extended time frame using novel human gut epithelium models. We demonstrate an increase in the numbers of adherent *C. difficile* accompanied by production of spores, toxins and bacterial filamentous forms,

138 along with host chemokine production, over 48h in a IEC monolayer VDC model. We demonstrate
139 that this system can be used to study interactions of obligate anaerobes such as the gut commensal,
140 *Bacteroides dorei*, with IECs. Interestingly, we show that *C. difficile* replication is significantly
141 reduced in presence of *B. dorei* on gut epithelial cells. In a complex 3-D model that we developed
142 which contains myofibroblasts on electrospun nanofiber scaffolds, we observed increased bacterial
143 adhesion to the IECs, compared to the 2-D model.
144
145 **RESULTS**
146 **Development of a gut cellular model for *C. difficile***
147 Polarized IECs (epithelial Caco-2 and mucus producing HT29-MTX goblet cells) were cultured
148 on the apical side of a Snapwell insert as shown in Figure 1. Inserts with polarized cell layers were
149 placed in the VDC and experiments were performed by perfusing a mixture of 5% CO_2 and 95%
150 air in the basolateral compartment for epithelial cell growth and an anaerobic gas mixture (10%
151 CO_2, 80% N_2 and 10% H_2) on the apical side for bacterial growth. After 3h, the cell layers were
152 washed with PBS, followed by the addition of fresh prereduced media (to simulate infection
153 conditions described below). The barrier integrity of IECs was monitored by measuring the
154 transepithelial electrical resistance (TEER). The TEER values demonstrated an intact epithelium
155 in the control IECs incubated within the VDC, although a slight decline was observed over 24h
156 (Figure 2A). However, no significant disruption to the IECs was seen after 24h or 48h by
157 microscopy; actin staining showed that the cytoskeleton of the control cells was intact at 24h and
158 48h (Figure 2B). Immunofluorescent staining of the Snapwell inserts for MUC2, a major mucus
159 protein produced by goblet cells, showed that a small amount of mucus was produced (Figure S1)
160 in this cell layer which contained 10% goblet cells (9 Caco-2:1 HT29-MTX).
161
162 Furthermore, to ensure that anaerobic conditions were maintained in the apical chamber, growth
163 of *C. difficile* in the apical compartment of the VDC was compared to growth in the anaerobic
164 cabinet for 3h and 24h. No negative impact on growth was observed at 3h and 24h compared to
165 bacteria grown in the anaerobic cabinet; instead, a slight increase in *C. difficile* growth in the VDC
166 was noted at 24h (Figure S2).
167
168 ***C. difficile* colonization leads to disruption of the intestinal epithelium**
169 To determine how *C. difficile* interacts with the human host in the short and long term, Caco-
170 2/HT29-MTX layers were infected with *C. difficile* R20291 at an MOI of 100:1 for different
171 periods of time in the anaerobic chamber of the VDC (Figure 1). In order to study bacteria that
172 adhere to the IECs and their replication, for all experiments, at 3h p.i., the apical supernatant
173 containing the *C. difficile* was removed, the IECs washed in PBS, fresh prereduced media added,
174 followed by incubation for the required time. Uninfected controls shown in Fig 2B were run in
175 parallel. The number of adherent *C. difficile* was determined by counting colony forming units
176 (CFUs) from the cell lysates, after washing off non-adherent bacteria. A significant increase in the
177 number of cell-associated *C. difficile* was observed from 3h to 24h p.i. (Figure 2C). This increase
178 in cell-associated bacteria corresponded to a decrease in TEER measurements indicating disruption
179 of the intestinal epithelial barrier (Figure 2A, Figure S3A). Confocal microscopy showed *C.*
180 *difficile* present as small micro-communities on the IECs at 24 and 48h (Fig 2D). An additional
181 image of microcommunities formed at 24h is shown in Fig S3B At early time points (3h and 6h
182 p.i.), there was little disruption of the actin filaments but at 24h and 48h p.i., destruction of the
183 cytoskeleton was evident (Figure 2D). Interestingly, at 48h p.i., immunofluorescent staining of

184 bacteria showed the presence of filamenting *C. difficile* (Figure 2D). A Coloc 2 ImageJ
185 colocalisation analysis revealed partial colocalisation of *C. difficile* with actin (Figure 2D) as
186 indicated by the Manders' M2 value (channel 2 for *C. difficile*) which shows 30% and 20% *C.*
187 *difficile* colocalised with the actin at 24h and 48h p.i respectively (Table 1) Positive Li's ICQ
188 values and Costes signifance test values (Table 1) further confirmed colocalisation at both time
189 points.
190
191 **Prolonged infection is associated with spore and toxin production, and host responses**
192 In order to fully understand bacterial factors necessary for CDI persistence, we studied the
193 production of spores, toxins and a host chemokine in the 2-D monolayer epithelial model. We
194 measured spores and total bacteria from the cell-associated fraction at different times after
195 infection. Although there were ~0.1% spores in the inoculum, there was a mild but significant
196 increase in spore numbers from 3h to 48h p.i. ($p < 0.05$, Figure 3A). After washing off the non-
197 adherent bacteria at 3h, we also tracked the bacterial spore numbers from 3h-48h in the
198 supernatants (Figure S4). By 48h p.i., there were equal numbers of spores and total cells in the
199 supernatants (Figure S4).
200
201 Toxins A and B (TcdA and TcdB) were monitored over time during infection using ELISA. Toxin
202 A increased significantly from 3h to 48h p.i. ($p < 0.05$) while low levels of toxin B were detected
203 at all times (Figure 3B). Analysis of the basolateral compartment supernatant for the host
204 chemokine IL-8, which has been previously implicated in *C. difficile* infection (Rao et al., 2014),
205 revealed that IL-8 levels were low at 6h p.i. but increased at 24h and 48h p.i. in this infection
206 model compared to uninfected controls (Figure 3C).
207
208 **Co-culturing *C. difficile* with *Bacteroides dorei* results in reduced *C. difficile* growth within**
209 **an epithelial gut model.**
210 To determine if our VDC-based system could be extended for use with other anaerobic bacteria,
211 we studied a strict commensal anaerobe, *B. dorei* within the epithelial monolayer model using
212 similar conditions as for *C. difficile*. Adherence to the IECs was determined at 3h and 24h by CFU
213 counts, as described for *C. difficile*. *B. dorei* adhered to the epithelial cells at 3h and multiplied
214 over 24h, as observed for *C. difficile* (Figure 4 A, B). A mixed culture of *B. dorei* and *C. difficile*
215 (1:1), prepared as described in Experimental Procedures was then cultured with the monolayer in
216 the VDC. Cell-associated bacteria were quantitated by plating on a medium used to selectively
217 isolate *C. difficile* colonies, which also allowed the growth of *B. dorei*. *Bacteroides* colonies were
218 distinguished by colony size, color and morphology (small colonies). A significant decrease in the
219 number of *C. difficile* was observed when co-cultured with *B. dorei* in the presence of IECs when
220 compared to mono-cultures of *C. difficile* at 24h p.i., but not at 3h p.i. (Figure 4A, B, $p < 0.001$).
221 We also observed higher colony counts when *B. dorei* was grown in co-culture with *C. difficile* at
222 3h and 24h, compared to mono-cultures of *B. dorei* (Figure 4A, B).
223
224 **Increased cell-associated bacteria in multilayer and 3-D models**
225 Typically, a myofibroblast layer underlies the basement membrane in the human gut. To develop
226 this system further by increasing its cell complexity, we incorporated myofibroblasts into our
227 model. Human CCD-18co myofibroblasts were first grown on the basolateral side of the polyester
228 Snapwell insert before seeding the IECs on the apical side (multilayer model, Figure 5A).
229 Furthermore, to recreate the highly porous architecture of the ECM in the basement membrane,

230 epithelial and fibroblasts cells were grown apically and basolaterally respectively on inserts
231 containing electrospun nanofiber scaffolds generated from polyethylene terephthalate to develop
232 a 3-D gut epithelium as reported previously (Morris et al., 2014). Scanning electron microscopy
233 revealed that these scaffolds exhibited a uniform nanofibrous matrix (Figure 5B) that supported
234 the attachment and proliferation of Caco-2 cells to form a confluent monolayer (Figure 5C) and
235 enabled the proliferation of the CCD-18co cells (Figure 5D). The average fiber diameter was 457
236 ± 170 nm (Figure S5).
237
238 Interestingly, in the multilayer model, we find that after infection with the same *C. difficile* strain,
239 same MOI's (100:1) and conditions as the monolayer model, for 3h and 24h (Figure 2), higher
240 numbers of bacteria adhered to the IECs at both time points (Figure 6A) compared to the
241 monolayer model without fibroblasts (Figure 2). Anti-fibronectin staining of the basolateral side
242 of the membrane containing the fibroblast cells indicated likely degradation of fibronectin, as
243 indicated by the destabilsed fibronectin network, and damage to the fibroblast layer at 24h p.i.
244 (Figure 6B). As before, immunofluorescent staining showed the localisation of *C. difficile* on the
245 epithelial cells at 3h and 24h p.i. (Figure 6C). Infections were not followed for longer times (48h)
246 as the cell layer was badly damaged by 24h p.i.
247
248 Similar to the multilayer model, we observed higher adhesion of *C. difficile* to the IECs at 3h and
249 24h p.i. in the 3-D gut epithelium (Figure 6D) compared to the 2-D model data in Figure 2.
250 Similarly, anti-fibronectin staining showed a destabilisation of the discrete fibronectin network
251 and likely cellular damage of the fibroblast layer in the 3-D model, as indicated by the lack of
252 discrete nuclear staining (Figure 6E). Confocal microscopy revealed the presence of numerous *C.*
253 *difficile* on the IECs at 24h p.i. (Figure 6F). Interestingly, at 24h p.i., immunofluorescent staining
254 showed the presence of filamenting *C. difficile* (Figure 6F), much earlier than seen in the
255 monolayer infection model. Bacterial staining did not always correlate to the CFU counts (Figure
256 6C and 6F), which we attribute to the loss of attached bacteria during the staining procedure.
257
258 **Spore, toxin and host chemokine production in response to *C. difficile* in 3-D and multilayer**
259 **models**
260 In both the 3-D and multilayer models of infection, spores were found to adhere to the epithelium
261 at numbers comparable to the 2-D monolayer model (Figure 7A, Figure 3A, Figure S6A), although
262 there was no increase in spore numbers over time. A higher increase in total cell numbers was
263 observed over time in the 3-D and multilayer model (Figure 7, Figure S6A), unlike the monolayer
264 model (Figure 3A). While there was higher variability, levels of toxin A in the apical compartment
265 supernatants from both models were comparable to that produced in the 2-D models (Figure 7B,
266 Figure S6B). Levels of toxin B detected in these models were also low (Figure 7B, Figure S6B).
267 Levels of IL-8 , increased over time (3-24h p.i.) in the 3-D (Figure 7C), and multilayer models
268 (Figure S6C), although these were not significantly different to the uninfected controls incubated
269 for 3h or 24h within the VDCs.
270
271 **DISCUSSION**
272 Attachment to the intestinal mucosa, subsequent multiplication and penetration of the gut
273 epithelium are generally essential for the establishment of a successful invasive infection (Kalita
274 et al., 2014; Ribet and Cossart, 2015). We report here the development of 2-D and 3-D *in vitro*
275 human gut models for studying interactions of obligate anaerobes with the host gut epithelium.

276 We have tracked *C. difficile* infection events over a prolonged time frame in an *in vitro* dual
277 environment human gut model. Along with demonstrating *C. difficile* adhesion, micro-
278 communities, toxin and spore production, we report formation of *C. difficile* filaments, a potential
279 adaptation mechanism during infection.
280
281 Previous *in vitro* infection models have shown the attachment of *C. difficile* on IECs either using
282 conditions that are not appropriate for the bacterium (such as growing in aerobic conditions) or
283 that are limited to short term infection due to the anaerobic growth requirements of *C. difficile*
284 (Cerquetti et al., 2002; Paredes-Sabja and Sarker, 2012; Jafari et al., 2016). However, in order to
285 study host-pathogen interactions at a molecular and cellular level, precise environmental control
286 and longer scales of infection are essential. The monolayer (2-D) gut epithelial model described
287 here is ideal for investigating molecular mechanisms underlying *C. difficile*-epithelial interactions
288 as it offers the ability to make cellular, immunological and molecular measurements along with
289 easy substitution of knockout cell lines and introduction of additional cellular components like
290 immune cells.
291
292 In the monolayer model, an increase in spores attached to the host cells was observed at 48h p.i.
293 indicating that spore formation occurs during *C. difficile* infection of the gut epithelium in our
294 monolayer model, as reported previously using mouse models (Deakin et al., 2012a). While we
295 cannot be sure if spores are formed and then adhere or if the vegetative cells adhere to the gut cells
296 and sporulate, our findings clearly support previous studies indicating spore adhesion to gut cells
297 during infection. *C. difficile* spores were reported to adhere to undifferentiated Caco-2 cells after
298 1h of infection as determined by viable spore counts and fluorescence microscopy (Paredes-Sabja
299 and Sarker, 2012), and recently, a spore surface protein CotE was shown to be essential for spore
300 binding to mucus producing epithelial cell layers (Hong et al., 2017).
301
302 Toxin production by *C. difficile* is known to play a role in pathogenesis by disrupting the barrier
303 integrity of the intestinal epithelium leading to increased permeability and re-organization of actin
304 (Aktories et al., 2017). Surprisingly, although there is a decrease in TEER and actin reorganization,
305 we detect very low levels of toxins at early time points of infection (6-24h). It is possible that low
306 toxin levels, particularly of toxin B, are sufficient to cause loss of the membrane integrity, as they
307 are augmented by other secreted enzymes produced by *C. difficile*. Although a partial bacterial
308 colocalisation with actin was observed later during infection (24 and 48h) we do not at present
309 understand if *C. difficile* mediates any direct interactions with the acin cytoskeleton. The formation
310 of *C. difficile* filaments seen at 24 and 48 p.i. may be associated with host cell contact and infection,
311 as our studies indicate that incubation in similar conditions (conditioned medium from infected
312 cells or growth in DMEM-10 for 48h) in the absence of cells does not induce this phenotype
313 (Figure S8A and S8B). *C. difficile* filaments may be important during infection, as seen for other
314 gut bacteria (Justice et al., 2008), although this needs to be investigated further.
315
316 More than 90% of the bacteria inhabiting the gut are obligate anaerobes but little is known about
317 the adhesion properties of individual bacteria to the intestinal epithelium. Previous research on
318 *Bacteroides fragilis*, a dominant bacterium isolated from intestinal tract infections showed that
319 bile salts enhance the adhesion to the intestinal epithelium and biofilm formation (Pumbwe et al.,
320 2007). However, for other dominant members of the Bacteroidetes phylum, there is insufficient
321 data as to how they interact with the gut epithelium. Our studies with *B. dorei*, a common gut

322 anaerobe in healthy individuals, demonstrates bacterial adhesion and multiplication on IECs, and
323 validates the utility of this *in vitro* model in studying host cell interactions of other anaerobic gut
324 bacteria.
325
326 While the gut microbiota is known to protect against *C. difficile* infection (Fuentes et al., 2014),
327 the direct interactions between commensals and gut pathogens have been poorly understood.
328 Although many genome sequencing studies have associated members of the Bacteroidetes with
329 healthy status, the roles of individual *Bacteroides* species in the gut remains unclear (Qin et al.,
330 2010; Huttenhower et al., 2012; Lloyd-Price et al., 2016). Recently, it was shown that *Bacteroides*
331 *ovatus* inhibited *C. difficile* growth in the presence of bile acids (Yoon et al., 2017). In this study,
332 we demonstrate suppression of gut cell-associated *C. difficile* growth by *B. dorei*, in the absence
333 of bile acids and in a physiologically relevant setting. Indeed, the reduction in *C. difficile* may be
334 because *B. dorei* competes better for nutrients, rather than a direct inhibition. In addition to host-
335 pathogen interactions, the models developed in this work allow three-way interaction studies
336 between commensals, pathogens and the host, i.e. the role of commensals in modulating effects of
337 pathogenic bacteria on the human host. Additionally, as these results may also suggest the potential
338 of non-spore forming anaerobic bacteria in suppressing *C. difficile* growth, such *in vitro* tools may
339 have value in screening and developing novel microbial therapies for treatment of *C. difficile* and
340 other anaerobic infections.
341
342 Three-dimensional models are known to promote more *in vivo*-like cell proliferation, growth
343 differentiation and cell-to cell contact (Kook et al., 2017). A recent study reported a 3-D intestinal
344 tissue model for *C. difficile*, where the authors demonstrated that *C. difficile* toxin activity was
345 higher in comparison to a 2-D transwell model (Shaban et al., 2018). They report that spores can
346 germinate into vegetative cells within this model, and that vegetative cells can survive upto 48h,
347 although the ability of *C. difficile* spores to germinate was similar in both their models. While both
348 their 3-D model and our models have epithelial and fibroblast cells, albeit with different scaffolds,
349 a key difference is the ability to control the apical and basolateral side environments using the
350 VDC, which may be important when performing sensitive molecular studies. Similar to Shaban et
351 al, we show bacterial replication upto 48h, although we also track bacteria that adhere to the
352 epithelial layer. Additionally, we have a nanofiber scaffold incorporated between the epithelial and
353 fibroflast layers, which creates a porous architecture similar to the basement membrane underlying
354 the gut epithelium, along with myofibroblast cells in the basal layer.
355
356 Previously, Morris *et al* showed that nanofibers were beneficial for epithelial cell differentiation
357 but not penetrable to fibroblasts (Morris et al., 2014). In addition to producing an ECM which
358 provides structural and biochemical support to cells, fibroblasts are also known to produce
359 chemokines when activated by bacteria (Smith et al., 1997). The increased *C. difficile* adhesion
360 observed in the multilayer and the 3-D models, which presumably leads to quicker progressing
361 infection, could be the result of indirect modulation of the epithelial barrier by the myofibroblast
362 cells, though at present we do not understand the underlying mechanisms. The increased amount
363 of the chemokine IL-8 observed in the uninfected 3-D and multilayer models could be attributed
364 to the myofibroblasts, although this chemokine response is not specific to *C. difficile* infection. It
365 is interesting to note that inspite of having higher numbers of bacteria attaching in these models,
366 there was no significant increase in the toxin levels. While we do not observe an increase in spore
367 numbers or distinct toxin production profiles in the 3-D and multilayer models, this may be due to

368 the quick progression of infection due to higher bacterial adhesion. We are currently optimising
369 these models using lower MOI's to enable longer infection experiments.
370
371 Both the multilayer and 3-D gut models have huge potential in studying *C. difficile* pathogenesis,
372 particularly for investigating host invasion and interactions with basolateral surface of the host
373 epithelium and are being utilized for studying functions of secreted *C. difficile* factors in the
374 laboratory. Overall, we have developed highly useful tools for studying *C. difficile* host-
375 interactions which we expect to have broad applications in studying anaerobic gut commensals
376 and their interactions with pathogens and the host.
377
378 **4 EXPERIMENTAL PROCEDURES**
379 *4.1 Bacterial strains and growth conditions*
380 *C. difficile* R20291 strain B1/NAP1/027 R20291 (isolated from the Stoke Mandeville outbreak in
381 2004 and 2005), was cultured on brain heart infusion (BHI) agar (Sigma-Aldrich, UK)
382 supplemented with 1 g/L cysteine (Sigma-Aldrich, UK), 5 g/L yeast extract under anaerobic
383 conditions (80% N_2, 10% CO_2, 10% H_2) in a Don Whitley workstation (Yorkshire, UK).
384
385 *4.2 Cell culture, media and conditions*
386 Intestinal epithelial cell line, Caco-2 (P6-P21) from American Type Culture Collection, mucus
387 producing cell line, HT29-MTX (P45-P56), gift from Nathalie Juge, Quadram Institute, Norwich,
388 and fibroblast cells, CCD-18co (P10-P17) were used. Caco-2 cells were grown in Dulbecco's
389 Modified Eagle Medium (DMEM) supplemented with 10% fetal bovine serum (FBS, Labtech,
390 UK), and 1% penicillin-streptomycin (10,000 units/mL penicillin, 10 mg/mL streptomycin,
391 Sigma-Aldrich, UK). HT29-MTX was grown in DMEM and CCD-18co in Eagle's Minimum
392 Essential Medium media. Both media were supplemented with 10% FBS, 1% penicillin-
393 streptomycin, 2 mM glutamine and 1% non-essential amino acids (Sigma-Aldrich, UK). All cell
394 lines were maintained in 5% CO_2 in a humidified incubator at 37°C and free from mycoplasma
395 contamination as determined by the EZ-PCR Mycoplasma kit (Biological Industries, USA).
396
397 For the epithelial 2-D models, Caco-2 and HT29-MTX were mixed in a 9:1 ratio and 2 x 10^5
398 cells/ml were seeded on a 12 mm Snapwell inserts (tissue culture treated polyester membrane,
399 Corning, New York, USA) supported by a detachable ring for 2 weeks to form a polarized
400 monolayer. For the multilayer and 3-D models, CCD-18co (1 X10^4 cells/ml) were first seeded on
401 the basolateral layer of the polyester Snapwell insert or electrospun nanofiber scaffold for 5 days
402 after which Caco-2 and HT29-MTX were seeded on the apical side as in the 2-D models for 14
403 days. Prior to the infection experiments, the cell culture medium in the Snapwell inserts was
404 replaced with antibiotic-free medium.
405
406 *4.3 Vertical diffusion chamber set up and measurement of transepithelial electrical resistance*
407 The Snapwell inserts containing the polarized cell layer were placed between the two half
408 chambers of the vertical diffusion chamber (Harvard Apparatus, Cambridge, UK) and sealed with
409 the provided clamps. 2.7 ml DMEM with 10% FBS (DMEM-10) was placed on both sides of the
410 chamber. Transepithelial electrical resistance measurements was performed using
411 Harvard/Navicyte electrodes on the EC-800 Epithelial Voltage Clamp (Harvard Apparatus,
412 Cambridge, UK) over 24h.
413

414 *4.4 Infection of intestinal epithelial cells (IECs) in 2-D, 3-D and multilayer models*
415 A single bacterial colony was inoculated in pre-reduced BHI broth (Oxoid, UK) supplemented
416 with 1 g/L cysteine (Sigma-Aldrich, UK) and 5 g/L yeast extract and incubated at 37ºC overnight.
417 The culture was centrifuged at 10,000g for 5 mins (Eppendorf 5810R) and bacterial pellet was
418 resuspended in DMEM-10 and incubated at 37ºC for at least an hour. Bacterial counts determined
419 from this culture were confirmed to be 2×10^7-3×10^7 CFU/ml for every experiment. This culture
420 was used to infect the IECs at a predetermined MOI of 100:1 in the apical side of the VDC
421 containing the IECs. The apical chamber was diffused with anaerobic gas mixture (10% CO_2,
422 10% H_2, 80% N_2, BOC, UK) and the basolateral compartment with 5% CO_2 and 95% air (BOC,
423 UK). At 3h p.i., the apical media containing the *C. difficile* was removed, the IECs washed in PBS
424 and 2.7 ml prereduced DMEM with 10% FBS added. It was incubated for a further 3h or up to
425 48h. The apical and basolateral media was then removed and stored at -80ºC. The IECs were
426 washed thrice in pre-reduced PBS before lysing in 1 ml sterile water. Serial dilutions prepared
427 from the IEC lysates were performed and plated on appropriate plates to determine the number of
428 cell-associated bacteria.
429
430 *4.5 Spore and total cell counts*
431 To determine the number of spores, the lysed cells and apical supernatants were heat treated at
432 65ºC for 20 mins as previously described (Fimlaid et al., 2015). Untreated and heat treated samples
433 were serial diluted and plated on BHI and BHI-T agar (supplemented with 0.1% sodium
434 taurocholate, Sigma-Aldrich, UK). No bacteria were obtained from the heat-treated samples plated
435 on BHI (without sodium taurocholate). The CFU/ml obtained from heat treated samples plated on
436 BHI-T plates represent heat-resistant spores, and the CFU/ml obtained from untreated samples
437 plated on BHI plates represent the total cell counts.
438
439 *4.6 Co-culture experiments*
440 For the co-culture experiments with *B. dorei*, both strains were grown to stationary phase overnight
441 in Schaedler anaerobic broth (Oxoid, UK), centrifuged with pellets resuspended in DMEM-10.
442 OD_{600} of the suspensions were measured but not used to normalize cultures, as we found that for
443 *B. dorei* the OD_{600} does not correlate well with CFU/ml. Both cultures were diluted 1:1 in DMEM-
444 10 before loading into the VDC. The CFU/ml of these diluted cultures were determined to ensure
445 that equal numbers of *C. difficile* to *B. dorei* (5×10^7- 2.9×10^8 CFU/ml) were present. Equal
446 volumes of the diluted cultures were mixed prior to loading into the VDC. An MOI of ~1000: 1
447 was used for both bacterial species. To differentiate *C. difficile* colonies from *B. dorei*, the BHIS
448 agar was supplemented with *C. difficile* selective supplement (Oxoid, UK).
449
450 *4.7 ELISA assays*
451 *C. difficile* toxin production was determined using the *C. difficile* toxin A or B kit by ELISA
452 following the manufacturer's instructions (tgcBIOMICS, Bingen am Rhein, Germany). Briefly,
453 the apical supernatants were centrifuged at 2500 g for 5 min and 100 µl of the supernatant in
454 duplicates was used for the assay. Duplicates (100 µl) of the standards (toxin A and B) provided
455 with the kit was run in the same ELISA assay as the apical supernatants from which the amount
456 of toxin produced was calculated. IL-8 production was also determined by analysis of basolateral
457 supernatants from VDC's using a human IL-8 ELISA kit (R&D systems, Minneapolis, USA)
458 following the manufacturer's instruction. Duplicates (100 µl) of the standards (IL-8) provided with

459 the kit was run in the same ELISA assay as the basolateral supernatants from which the amount of
460 IL-8 produced was calculated.
461
462 *4.8 Electrospinning protocol*
463 Electrospinning procedure was performed as described previously (Morris et al., 2014). Briefly,
464 scaffolds were produced by dissolving polyethylene terephthalate (PET, from food grade drinking
465 bottles) in equal ratio of trifluoroacetic acid and dichloromethane (1:1) to create a 10% (w/v) PET
466 solution to produce the nanofiber scaffolds. Electrospinning processing parameters included an
467 applied voltage of 14kV, a tip-collector distance (TCD) of 15cm, a flow rate of 0.5 ml/h and an 18
468 gauge spinneret for a period of 2h. Electrospinning was conducted at ambient conditions in a
469 ducted fume hood with fibers collected on a stainless steel rotating drum (50 rpm). Once collected,
470 the scaffolds were stored in aluminum foil at room temperature until required. Prior to cell culture,
471 scaffolds were positioned in 12 mm Snapwell inserts (Corning, New York, USA) by replacing the
472 commercial membrane with the electrospun nanofiber matrix. PET scaffolds were cut into 2.5 cm
473 diameter circles and fixed with Costar Snapwell
474 inserts using aquarium sealant glue (King British, Beaphar Company). They were sterilized by
475 exposing to UV at the power of 80 mJ/cm^2 for 15 minutes on each side using a UV lamp (CL-1000
476 Ultraviolet Crosslinker) and soaking in 10x antibiotic-antimycotic solution (final concentration:
477 1,000 units/ml penicillin, 1 mg/ml streptomycin and 2.5 µg/ml amphotericin B, Sigma Aldrich,
478 UK) for 3h at 25 °C. Antibiotic-antimycotic solution was then removed and the scaffolds were
479 washed with PBS (pH 7.4) three times. The scaffolds were air-dried in the microbiological class 2
480 safety cabinet overnight.
481
482 *4.9 Scanning Electron Microscopy (SEM)*
483 The fiber morphology of the nanofiber scaffolds was assessed using SEM. Acellular samples were
484 sputter coated (Leica EMSCD005) with gold for 4-5 mins prior to microscopy. Scaffolds seeded
485 with cells were fixed in 3% (v/v) glutaraldehyde overnight at 4°C. Samples were washed thrice in
486 PBS and dehydrated through a series of industrial methylated spirits (IMS) concentrations diluted
487 in water (25-100% v/v) for 10 mins each. Following dehydration, hexamethyldisilazane (HMDS)
488 was added to chemically dry the samples, this process was then repeated and the samples allowed
489 to air dry overnight before sputter coating as described above. Scaffold and cell morphology was
490 observed at various magnifications as indicated on the scale bar of the images (JEOL JSM-6100,
491 JEOL, UK). Images were processed using ImageJ software (W. Rasband, National Institute of
492 Health, USA) to determine the fiber diameter and 150 measurements (50 measurements per
493 scaffold) from 3 independently produced scaffolds were assessed.
494
495 *4.10 Immunofluorescence assays and imaging*
496 The Snapwell inserts, containing either the commercial membrane or PET nanofiber scaffold, were
497 fixed in 4% PFA for 15 min, washed in PBS, permeabilized with 1% saponin (Sigma-Aldrich,
498 UK) in 0.3% triton X-100 (Fisher Scientific, UK) and thereafter blocked against non-specific
499 antibody binding with 3% BSA in PBS (Sigma-Aldrich, UK). For staining *C. difficile*, infected
500 cells were incubated with anti-*C. difficile* serum for 1h, followed by Alexa Fluor 488 goat anti-
501 rabbit secondary antibody (New England Biolabs, UK) for 1h. Alexa fluor phalloidin 647 was used
502 to stain the actin cytoskeleton and cell nuclei were stained with ProLong Gold Antifade mountant
503 containing 4,6-diamidino-2-phenylindole (DAPI) (New England Biolabs, UK). To determine
504 mucus production, the Snapwell inserts were fixed, permeabilized and blocked as described above.

The Snapwell insert was incubated with mucin 2 anti-rabbit primary antibody (Santa Cruz Biotechnology, US) overnight at 4ºC followed by Alexa Fluor 488 goat anti-rabbit secondary antibody (New England Biolabs, UK) for 1h. Images were taken using a confocal spinning-disk microscope (VOX UltraView, PerkinElmer, UK) with a 40X oil objective and two Hamamatsu ORCA-R2 cameras, by Volocity 6.0 (PerkinElmer, UK). Post-image analysis was performed with ImageJ software.

4.11 Colocalisation analysis

Coloc 2 from the ImageJ software was used to determine the colocalisation between *C. difficile,* visualized in green and actin in red, from 4 independent images at 24h and 48h p.i. Coloc 2 runs several intensity based colocalisation tests such as Manders correlation (Manders, 1993), Li intensity correlation quotient (ICQ) (Li et al., 2004) and Costes significance test (Costes et al., 2004). Intensity based analysis such as Manders' showed the level of colocalisation between the two channels (channel 1 for actin and 2 for *C. difficile*). Manders' output two results, M1 and M2 describe the colocalisation coefficients of the two channels. Manders' M1 value showed that an average of 50% actin colocalised with *C.difficile* and Manders' M2 value indicated that 100% of the *C. difficile* colocalised with actin at 24h p.i (values between 0.5 - 1). At 48h p.i, Manders M1 and M2 values showed that 100% of the actin colocalised with *C. difficile*. After applying an automatic threshold determined by the software, the levels of colocalisation was lower (Table S1). One hundred randomizations were used to determine the Costes significant P value. The Costes P value if > 95% or 0.95 was deemed to be significant. For all analyses except the Li ICQ, 1 represents perfect colocalisation with lesser values indicating the various degree of colocalisation. For the Li ICQ, the values range from maximum 0.5 to -0.5, i.e. with random (or mixed) staining ICQ= ~0; dependent staining $0 < ICQ \leq +0.5$, and for segregated staining $0 > ICQ \geq - 0.5$ (Li et al., 2004).

4.12 Statistical analysis

One-way or two-way anova was used to compare two or more groups when there was one or more independent variables respectively with Tukey's test for multiple comparison using Graphpad Prism. Student t test (two tailed) was used to determine the significance between two groups. Significance is represented as $*p < 0.05$, $**p < 0.01$, $***p < 0.001$ and $****p < 0.0001$. Except stated otherwise, all the results presented are the average of 3 independent experiments performed in duplicates or triplicates. The error bars indicate the standard deviation (SD).

ACKNOWLEDGEMENTS: We thank Trevor Lawley for providing *C. difficile* strains and Nathalie Juge for providing the HT29-MTX cell line. We thank Arnaud Kengmo Tchoupa for reading the manuscript.

Author contributions statement: BA, JH, JP performed experiments for this study. UD and AA produced the nanofiber scaffolds. MU, FR and SS were involved in designing experiments in the study. BA and MU wrote the main manuscript and all authors reviewed the manuscript.

Funding: This work is funded by the Wellcome Trust Seed Award in Science to MU (grant no 108263/Z/15/Z) and a Synthetic Biology PhD funded by BBSRC & EPSRC, grant number: EP/L016494/1 to JH. This grant was awarded to the Warwick Integrative Synthetic Biology

Centre (grant ref: BB/M017982/1) funded under the UK Research Councils' Synthetic Biology for Growth programme.

Conflict of interest statement: The authors declare no competing interests.

REFERENCES

Adamu, B.O., and Lawley, T.D. (2013). Bacteriotherapy for the treatment of intestinal dysbiosis caused by *Clostridium difficile* infection. *Current Opinion in Microbiology* 16(5)**,** 596-601. doi: 10.1016/j.mib.2013.06.009.

Aktories, K., Schwan, C., and Jank, T. (2017). *Clostridium difficile* Toxin Biology. *Annual Review of Microbiology* 71(1)**,** 281-307. doi: 10.1146/annurev-micro-090816-093458.

Barketi-Klai, A., Hoys, S., Lambert-Bordes, S., Collignon, A., and Kansau, I. (2011). Role of fibronectin-binding protein A in *Clostridium difficile* intestinal colonization. *Journal of Medical Microbiology* 60(8)**,** 1155-1161. doi: doi:10.1099/jmm.0.029553-0.

Barrila, J., Yang, J., Crabbé, A., Sarker, S.F., Liu, Y., Ott, C.M., et al. (2017). Three-dimensional organotypic co-culture model of intestinal epithelial cells and macrophages to study *Salmonella enterica* colonization patterns. *npj Microgravity* 3(1)**,** 10. doi: 10.1038/s41526-017-0011-2.

Batah, J., Kobeissy, H., Bui Pham, P.T., Deneve-Larrazet, C., Kuehne, S., Collignon, A., et al. (2017). *Clostridium difficile* flagella induce a pro-inflammatory response in intestinal epithelium of mice in cooperation with toxins. *Sci Rep* 7(1)**,** 3256. doi: 10.1038/s41598-017-03621-z.

Bobo, L.D., El Feghaly, R.E., Chen, Y.S., Dubberke, E.R., Han, Z., Baker, A.H., et al. (2013). MAPK-activated protein kinase 2 contributes to Clostridium difficile-associated inflammation. *Infect Immun* 81(3)**,** 713-722. doi: 10.1128/IAI.00186-12.

Calabi, E., Calabi, F., Phillips, A.D., and Fairweather, N.F. (2002). Binding of *Clostridium difficile* Surface Layer Proteins to Gastrointestinal Tissues. *Infection and Immunity* 70(10)**,** 5770-5778. doi: 10.1128/iai.70.10.5770-5778.2002.

Carter, G.P., Chakravorty, A., Pham Nguyen, T.A., Mileto, S., Schreiber, F., Li, L., et al. (2015). Defining the Roles of TcdA and TcdB in Localized Gastrointestinal Disease, Systemic Organ Damage, and the Host Response during Clostridium difficile Infections. *MBio* 6(3)**,** e00551. doi: 10.1128/mBio.00551-15.

Cerquetti, M., Serafino, A., Sebastianelli, A., and Mastrantonio, P. (2002). Binding of *Clostridium difficile* to Caco-2 epithelial cell line and to extracellular matrix proteins. *FEMS Immunology & Medical Microbiology* 32(3)**,** 211-218. doi: 10.1111/j.1574-695X.2002.tb00556.x.

Chen, S., Sun, C., Wang, H., and Wang, J. (2015). The Role of Rho GTPases in Toxicity of Clostridium difficile Toxins. *Toxins (Basel)* 7(12)**,** 5254-5267. doi: 10.3390/toxins7124874.

Chen, X., Katchar, K., Goldsmith, J.D., Nanthakumar, N., Cheknis, A., Gerding, D.N., et al. (2008). A mouse model of Clostridium difficile-associated disease. *Gastroenterology* 135(6)**,** 1984-1992. doi: 10.1053/j.gastro.2008.09.002.

Collins, D.A., Selvey, L.A., Celenza, A., and Riley, T.V. (2017). Community-associated *Clostridium difficile* infection in emergency department patients in Western Australia. *Anaerobe* 48(Supplement C)**,** 121-125. doi: https://doi.org/10.1016/j.anaerobe.2017.08.008.

596 Costes, S.V., Daelemans, D., Cho, E.H., Dobbin, Z., Pavlakis, G., and Lockett, S. (2004).
597 Automatic and quantitative measurement of protein-protein colocalization in live cells.
598 *Biophys J* 86(6)**,** 3993-4003. doi: 10.1529/biophysj.103.038422.
599 Darkoh, C., Odo, C., and DuPont, H.L. (2016). Accessory Gene Regulator-1 Locus Is Essential
600 for Virulence and Pathogenesis of Clostridium difficile. *MBio* 7(4). doi:
601 10.1128/mBio.01237-16.
602 Davies, K.A., Longshaw, C.M., Davis, G.L., Bouza, E., Barbut, F., Barna, Z., et al. (2014).
603 Underdiagnosis of *Clostridium difficile* across Europe: the European, multicentre,
604 prospective, biannual, point-prevalence study of *Clostridium difficile* infection in
605 hospitalised patients with diarrhoea (EUCLID). *The Lancet Infectious Diseases* 14(12)**,**
606 1208-1219. doi: 10.1016/S1473-3099(14)70991-0.
607 Deakin, L.J., Clare, S., Fagan, R.P., Dawson, L.F., Pickard, D.J., West, M.R., et al. (2012a). The
608 *Clostridium difficile* spo0A Gene Is a Persistence and Transmission Factor. *Infection and*
609 *Immunity* 80(8)**,** 2704-2711. doi: 10.1128/iai.00147-12.
610 Deakin, L.J., Clare, S., Fagan, R.P., Dawson, L.F., Pickard, D.J., West, M.R., et al. (2012b).
611 Clostridium difficile spo0A gene is a persistence and transmission factor. *Infect Immun*.
612 doi: 10.1128/IAI.00147-12.
613 DeCicco RePass, M.A., Chen, Y., Lin, Y., Zhou, W., Kaplan, D.L., and Ward, H.D. (2017).
614 Novel Bioengineered Three-Dimensional Human Intestinal Model for Long-Term
615 Infection of *Cryptosporidium parvum*. *Infection and Immunity* 85(3)**,** e00731-00716. doi:
616 10.1128/IAI.00731-16.
617 Drummond, C.G., Nickerson, C.A., and Coyne, C.B. (2016). A Three-Dimensional Cell Culture
618 Model To Study Enterovirus Infection of Polarized Intestinal Epithelial Cells. *mSphere*
619 1(1). doi: 10.1128/mSphere.00030-15.
620 England, P.H. (2017). Annual Epidemiological Commentary: Mandatory MRSA, MSSA and E.
621 coli bacteraemia and C. difficile infection data, 2016/17. .
622 Fimlaid, K.A., Jensen, O., Donnelly, M.L., Siegrist, M.S., and Shen, A. (2015). Regulation of
623 Clostridium difficile Spore Formation by the SpoIIQ and SpoIIIA Proteins. *PLoS Genet*
624 11(10)**,** e1005562. doi: 10.1371/journal.pgen.1005562.
625 Fuentes, S., van Nood, E., Tims, S., Heikamp-de Jong, I., ter Braak, C.J.F., Keller, J.J., et al.
626 (2014). Reset of a critically disturbed microbial ecosystem: faecal transplant in recurrent
627 *Clostridium difficile* infection. *The ISME Journal* 8(8)**,** 1621-1633. doi:
628 10.1038/ismej.2014.13.
629 Gravel, D., Miller, M., Simor, A., Taylor, G., Gardam, M., McGeer, A., et al. (2009). Health
630 Care-Associated Clostridium difficile Infection in Adults Admitted to Acute Care
631 Hospitals in Canada: A Canadian Nosocomial Infection Surveillance Program Study.
632 *Clin Infect Dis* 48. doi: 10.1086/596703.
633 Hennequin, C., Porcheray, F., Waligora-Dupriet, A.-J., Collignon, A., Barc, M.-C., Bourlioux,
634 P., et al. (2001). GroEL (Hsp60) of *Clostridium difficile* is involved in cell adherence.
635 *Microbiology* 147(1)**,** 87-96. doi: 10.1099/00221287-147-1-87.
636 Hong, H.A., Ferreira, W.T., Hosseini, S., Anwar, S., Hitri, K., Wilkinson, A.J., et al. (2017). The
637 Spore Coat Protein CotE Facilitates Host Colonization by Clostridium difficile. *J Infect*
638 *Dis* 216(11)**,** 1452-1459. doi: 10.1093/infdis/jix488.
639 Huttenhower, C., Gevers, D., Knight, R., Abubucker, S., Badger, J.H., Chinwalla, A.T., et al.
640 (2012). Structure, function and diversity of the healthy human microbiome. *Nature*
641 486(7402)**,** 207.

642 Jafari, N.V., Kuehne, S.A., Minton, N.P., Allan, E., and Bajaj-Elliott, M. (2016). *Clostridium*
643 *difficile*-mediated effects on human intestinal epithelia: Modelling host-pathogen
644 interactions in a vertical diffusion chamber. *Anaerobe* 37(Supplement C)**,** 96-102. doi:
645 https://doi.org/10.1016/j.anaerobe.2015.12.007.
646 Janvilisri, T., Scaria, J., and Chang, Y.-F. (2010). Transcriptional profiling of *Clostridium*
647 *difficile* and Caco-2 cells during infection. *The Journal of infectious diseases* 202(2)**,** 282-
648 290. doi: 10.1086/653484.
649 Justice, S.S., Hunstad, D.A., Cegelski, L., and Hultgren, S.J. (2008). Morphological plasticity as
650 a bacterial survival strategy. *Nat Rev Micro* 6(2)**,** 162-168.
651 Kalita, A., Hu, J., and Torres, A.G. (2014). Recent advances in adherence and invasion of
652 pathogenic Escherichia coli. *Curr Opin Infect Dis* 27(5)**,** 459-464. doi:
653 10.1097/QCO.0000000000000092.
654 Kasendra, M., Barrile, R., Leuzzi, R., and Soriani, M. (2014). *Clostridium difficile* Toxins
655 Facilitate Bacterial Colonization by Modulating the Fence and Gate Function of Colonic
656 Epithelium. *Journal of Infectious Diseases* 209(7)**,** 1095-1104. doi: 10.1093/infdis/jit617.
657 Kook, Y.-M., Jeong, Y., Lee, K., and Koh, W.-G. (2017). Design of biomimetic cellular
658 scaffolds for co-culture system and their application. *Journal of Tissue Engineering* 8**,**
659 2041731417724640. doi: 10.1177/2041731417724640.
660 Kovacs-Simon, A., Leuzzi, R., Kasendra, M., Minton, N., Titball, R.W., and Michell, S.L.
661 (2014). Lipoprotein CD0873 Is a Novel Adhesin of *Clostridium difficile*. *The Journal of*
662 *Infectious Diseases* 210(2)**,** 274-284. doi: 10.1093/infdis/jiu070.
663 Kuehne, S.A., Cartman, S.T., Heap, J.T., Kelly, M.L., Cockayne, A., and Minton, N.P. (2010).
664 The role of toxin A and toxin B in *Clostridium difficile* infection. *Nature* 467(7316)**,** 711-
665 713. doi: 10.1038/nature09397.
666 Kuehne, S.A., Collery, M.M., Kelly, M.L., Cartman, S.T., Cockayne, A., and Minton, N.P.
667 (2013). Importance of toxin A, toxin B, and CDT in virulence of an epidemic *Clostridium*
668 *difficile* strain. *The Journal of infectious diseases* 209(1)**,** 83-86.
669 Kuehne, S.A., Collery, M.M., Kelly, M.L., Cartman, S.T., Cockayne, A., and Minton, N.P.
670 (2014). Importance of toxin A, toxin B, and CDT in virulence of an epidemic Clostridium
671 difficile strain. *J Infect Dis* 209(1)**,** 83-86. doi: 10.1093/infdis/jit426.
672 Lawley, T.D., Clare, S., Deakin, L.J., Goulding, D., Yen, J.L., Raisen, C., et al. (2010). Use of
673 Purified *Clostridium difficile* Spores To Facilitate Evaluation of Health Care Disinfection
674 Regimens. *Applied and Environmental Microbiology* 76(20)**,** 6895-6900. doi:
675 10.1128/aem.00718-10.
676 Leslie, J.L., Huang, S., Opp, J.S., Nagy, M.S., Kobayashi, M., Young, V.B., et al. (2015).
677 Persistence and Toxin Production by *Clostridium difficile* within Human Intestinal
678 Organoids Result in Disruption of Epithelial Paracellular Barrier Function. *Infection and*
679 *Immunity* 83(1)**,** 138-145. doi: 10.1128/iai.02561-14.
680 Lessa, F.C., Mu, Y., Bamberg, W.M., Beldavs, Z.G., Dumyati, G.K., Dunn, J.R., et al. (2015).
681 Burden of *Clostridium difficile* infection in the United States. *N Engl J Med* 372. doi:
682 10.1056/NEJMoa1408913.
683 Li, Q., Lau, A., Morris, T.J., Guo, L., Fordyce, C.B., and Stanley, E.F. (2004). A syntaxin 1,
684 Galpha(o), and N-type calcium channel complex at a presynaptic nerve terminal: analysis
685 by quantitative immunocolocalization. *J Neurosci* 24(16)**,** 4070-4081. doi:
686 10.1523/JNEUROSCI.0346-04.2004.

687 Lloyd-Price, J., Abu-Ali, G., and Huttenhower, C. (2016). The healthy human microbiome.
688 *Genome Medicine* 8.
689 Lyras, D., O'Connor, J.R., Howarth, P.M., Sambol, S.P., Carter, G.P., Phumoonna, T., et al.
690 (2009). Toxin B is essential for virulence of Clostridium difficile. *Nature* 458(7242)**,**
691 1176-1179. doi: 10.1038/nature07822.
692 Manders, E.M., Verbeek, F. J. and Aten J.A (1993). Measurement of co-localization of objects
693 in dual-colour confocal images. *Journal of Microcopy* 169(3)**,** 375-382.
694 McKee, R.W., Aleksanyan, N., Garrett, E.M., and Tamayo, R. (2018). Type IV Pili Promote
695 Clostridium difficile Adherence and Persistence in a Mouse Model of Infection. *Infect*
696 *Immun* 86(5). doi: 10.1128/IAI.00943-17.
697 Merrigan, M.M., Venugopal, A., Roxas, J.L., Anwar, F., Mallozzi, M.J., Roxas, B.A.P., et al.
698 (2013). Surface-Layer Protein A (SlpA) Is a Major Contributor to Host-Cell Adherence
699 of *Clostridium difficile*. *PLOS ONE* 8(11)**,** e78404. doi: 10.1371/journal.pone.0078404.
700 Mills, D.C., Gundogdu, O., Elmi, A., Bajaj-Elliott, M., Taylor, P.W., Wren, B.W., et al. (2012).
701 Increase in *Campylobacter jejuni* Invasion of Intestinal Epithelial Cells under Low-
702 Oxygen Coculture Conditions That Reflect the In Vivo Environment. *Infection and*
703 *Immunity* 80(5)**,** 1690-1698. doi: 10.1128/iai.06176-11.
704 Mora-Uribe, P., Miranda-Cárdenas, C., Castro-Córdova, P., Gil, F., Calderón, I., Fuentes, J.A., et
705 al. (2016). Characterization of the Adherence of *Clostridium difficile* Spores: The
706 Integrity of the Outermost Layer Affects Adherence Properties of Spores of the Epidemic
707 Strain R20291 to Components of the Intestinal Mucosa. *Frontiers in Cellular and*
708 *Infection Microbiology* 6**,** 99. doi: 10.3389/fcimb.2016.00099.
709 Morris, G.E., Bridge, J.C., Brace, L.A., Knox, A.J., Aylott, J.W., Brightling, C.E., et al. (2014).
710 A novel electrospun biphasic scaffold provides optimal three-dimensional topography for
711 in vitro co-culture of airway epithelial and fibroblast cells. *Biofabrication* 6(3)**,** 035014.
712 doi: 10.1088/1758-5082/6/3/035014.
713 Paredes-Sabja, D., and Sarker, M.R. (2012). Adherence of *Clostridium difficile* spores to Caco-2
714 cells in culture. *Journal of Medical Microbiology* 61(9)**,** 1208-1218. doi:
715 doi:10.1099/jmm.0.043687-0.
716 Pumbwe, L., Skilbeck, C.A., Nakano, V., Avila-Campos, M.J., Piazza, R.M.F., and Wexler,
717 H.M. (2007). Bile salts enhance bacterial co-aggregation, bacterial-intestinal epithelial
718 cell adhesion, biofilm formation and antimicrobial resistance of *Bacteroides fragilis*.
719 *Microbial Pathogenesis* 43(2)**,** 78-87. doi: https://doi.org/10.1016/j.micpath.2007.04.002.
720 Qin, J., Li, R., Raes, J., Arumugam, M., Burgdorf, K.S., and Manichanh, C. (2010). A human gut
721 microbial gene catalogue established by metagenomic sequencing. *Nature* 464. doi:
722 10.1038/nature08821.
723 Rao, K., Erb-Downward, J.R., Walk, S.T., Micic, D., Falkowski, N., Santhosh, K., et al. (2014).
724 The systemic inflammatory response to *Clostridium difficile* infection. *PLoS One* 9(3)**,**
725 e92578.
726 Ravi, M., Paramesh, V., Kaviya, S.R., Anuradha, E., and Solomon, F.D.P. (2015). 3D Cell
727 Culture Systems: Advantages and Applications. *Journal of Cellular Physiology* 230(1)**,**
728 16-26. doi: 10.1002/jcp.24683.
729 Ribet, D., and Cossart, P. (2015). How bacterial pathogens colonize their hosts and invade
730 deeper tissues. *Microbes Infect* 17(3)**,** 173-183. doi: 10.1016/j.micinf.2015.01.004.
731 Schüller, S., and Phillips, A.D. (2010). Microaerobic conditions enhance type III secretion and
732 adherence of enterohaemorrhagic *Escherichia coli* to polarized human intestinal

epithelial cells. *Environmental Microbiology* 12(9)**,** 2426-2435. doi: 10.1111/j.1462-2920.2010.02216.x.

Shaban, L., Chen, Y., Fasciano, A.C., Lin, Y., Kaplan, D.L., Kumamoto, C.A., et al. (2018). A 3D intestinal tissue model supports Clostridioides difficile germination, colonization, toxin production and epithelial damage. *Anaerobe* 50**,** 85-92. doi: 10.1016/j.anaerobe.2018.02.006.

Smith, R.S., Smith, T.J., Blieden, T.M., and Phipps, R.P. (1997). Fibroblasts as sentinel cells. Synthesis of chemokines and regulation of inflammation. *The American Journal of Pathology* 151(2)**,** 317-322.

Tasteyre, A., Barc, M.-C., Collignon, A., Boureau, H., and Karjalainen, T. (2001). Role of FliC and FliD Flagellar Proteins of *Clostridium difficile* in Adherence and Gut Colonization. *Infection and Immunity* 69(12)**,** 7937-7940. doi: 10.1128/iai.69.12.7937-7940.2001.

Vohra, P., and Poxton, I.R. (2011). Efficacy of decontaminants and disinfectants against *Clostridium difficile*. *Journal of Medical Microbiology* 60(8)**,** 1218-1224. doi: doi:10.1099/jmm.0.030288-0.

Waligora, A.-J., Hennequin, C., Mullany, P., Bourlioux, P., Collignon, A., and Karjalainen, T. (2001). Characterization of a Cell Surface Protein of *Clostridium difficile* with Adhesive Properties. *Infection and Immunity* 69(4)**,** 2144-2153. doi: 10.1128/iai.69.4.2144-2153.2001.

Yoon, S., Yu, J., McDowell, A., Kim, S.H., You, H.J., and Ko, G. (2017). Bile salt hydrolase-mediated inhibitory effect of *Bacteroides ovatus* on growth of *Clostridium difficile. Journal of Microbiology* 55(11)**,** 892-899. doi: 10.1007/s12275-017-7340-4.

Figure legends

Figure 1. Scheme for generation of epithelial layers for use within vertical diffusion chambers. For the 2-D model, intestinal epithelial cells were grown to form a polarized confluent monolayer in a Snapwell insert for 2 weeks before inserting in the VDCs. *C. difficile* was added to the apical chamber which was perfused with an anaerobic gas mix and incubated for different times while maintaining anaerobic conditions. The basolateral compartment was perfused with a mixture of 5% CO_2 and 95% air, necessary for growth of IECs.

Figure 2. The VDC permits growth of host cells and enables *C. difficile* to adhere to gut epithelial cells. (A) Reduction in TEER measurements at different time after infection indicating increasing permeability compared to uninfected controls, $^{**}p < 0.01$, $^{****}p < 0.0001$ as determined by one-way ANOVA. (B) Immunofluorescent microscopy images of uninfected controls at 24h and 48h. Actin is stained with phalloidin (red) and cell nuclei are stained with DAPI (blue), scale bar =10 μM. (C) Colony counts from infected cell lysates to determine the number of adherent or cell-associated bacteria. A significant increase in adherent *C. difficile* is observed from 3h to 24h. Data shown is the mean of 3 independent experiments in triplicates and error bars indicate SD, $^{*}p < 0.05$ and $^{****}p < 0.0001$ as determined by one-way ANOVA. (D) Immunofluorescent microscopy images of *C. difficile* infected IECs at 3h, 6h, 24h and 48h p.i. showing colocalisation (yellow) of the bacteria stained with anti *C. difficile* antibodies (green) with actin, stained with phalloidin (red). Cell nuclei are stained with DAPI (blue). Reorganization and destruction of actin filaments is observed at 24h and 48h p.i. Inset (white square box) shows micro-communities, and bacterial colocalisation with actin at 24h and 48h (yellow) and *C. difficile*

filamentous forms observed at 48h p.i. are indicated by white arrows, scale bar =10 μM. Inset below shows the orthogonal XZ axis view of the IECs.

Figure 3. Production of *C. difficile* spores, toxins and host responses to infection. (A) Colony counts of spores recovered after heat treatment, and total cells in the cell-associated *C. difficile* fraction (infected cell lysates) in the 2-D epithelial model. Data shown is the mean of 3 independent experiments and error bars indicate SD, $*p < 0.05$ as determined by two-way ANOVA (B) ELISA for *C. difficile* toxins A and B shows increased toxin production after extended infection. Toxins were measured from medium obtained from the apical compartment containing uninfected cell layers incubated for 24h or 48h (Control) or cells infected with *C. difficile* for 3h, 6h, 24h or 48h. Data shown is the mean of 3 independent experiments and error bars indicate SD, $*p < 0.05$ as determined by two-way ANOVA. Grey line represents the sensitivity of the test at 0.5 ng/ml. (C). ELISA for human IL-8 indicates increased IL-8 production at 24h and 48h p.i. IL-8 was measured in medium obtained from the basolateral compartment containing uninfected cell layers incubated for 3h, 6h, 24h or 48h (Control) or cells infected with *C. difficile* for 3h-48h. Grey line represents the limit of detection at 32 pg/ml. Data shown is the mean of 3 independent experiments and error bars indicate SD, $*p < 0.05$, $**p < 0.01$ and $***p < 0.001$, $p < 0.0001$ as determined by one-way ANOVA.

Figure 4. Studying *C. difficile*-commensal interactions within epithelial models. (A) Mono or mixed cultures of *B. dorei* and *C. difficile* were incubated with the epithelial monolayers in VDCs for 3h. Co–cultures of *B. dorei* with *C. difficile* in the VDC showed no significant reduction of *C. difficile* growth at 3h p.i. as compared to *C. difficile* mono-culture. A relative increase in *B. dorei* adhering to the IECs was observed in co-cultures. 'Co-culture Bd and Cd' represents the growth of *B. dorei* and *C. difficile* respectively in the mixed culture (Bd, *B. dorei* and Cd, *C. difficile*) on the IECs. Data shown is the mean of 3 independent experiments and error bars indicate SD, $***p < 0.001$, ns, not significant as determined by one-way ANOVA. (B) At 24h, a significant reduction of *C. difficile* CFU is observed in co-cultures compared with *C. difficile* mono-culture. Data shown is the mean of 3 independent experiments and error bars indicate SD, $***p < 0.001$, ns, not significant as determined by one-way ANOVA.

Figure 5. Scheme for generation of multilayer and 3-D models containing fibroblast cells and cell growth on the electrospun nanofibrous matrix (A) Fibroblast cells were first seeded on the basolateral side of the Snapwell or nanofiber scaffold for the multilayer and 3-D models for 5 days. Thereafter, IECs were cultured on the apical side for 2 weeks before placing the Snapwell insert between two halves of the chamber. *C. difficile* was infected apically while maintaining anaerobic conditions and the basolateral compartment was perfused with 5% CO_2 and 95% air. (B) Polyethylene terephthalate (PET; 10% w/v) was electrospun and exhibited a uniform nanofibrous matrix as determined by scanning electron microscopy. (C) Caco-2 epithelial cells were able to form a confluent monolayer on the nanofibrous scaffolds (the scaffold can be seen underneath the cells following processing for SEM). (D) The CCD-18co cells proliferated across the nanofibrous scaffold forming cell processes to adhere to the nanofibers.

Figure 6. Infection of *C. difficile* in multilayer and 3-D model leads to increased adhesion. Increased adherence of *C. difficile* in the multilayer and 3-D models, where fibroblasts are grown as a basolateral layer on polyester and nanofibers respectively. (A) Serial dilutions of the infected

825 epithelial cell lysates were plated to determine the number of cell-associated bacteria in the
826 multilayer model. Data shown is the mean of 3 independent experiments and error bars indicate
827 SD, ns, not significant as determined by student t test (B) Anti-fibronectin (green) staining of
828 fibroblast cells in the basolateral layer of the control at 24h p.i and infected cells at 3h and 24h p.i.
829 showing redistribution of fibronectin, damaged fibroblast layer in the multilayer model, as
830 indicated by a white arrow. (C) Representative images of *C. difficile* on the apical layer at 3h and
831 24h p.i. Inset below shows the orthogonal XZ axis view of the IECs. *C. difficile* is stained green,
832 actin, red and cell nuclei, blue, Scale bar = 10 μM. (D) *C. difficile* colony counts from the 3-D
833 model infected cell lysates. Data shown is the mean of 3 independent experiments and error bars
834 indicate SD, ns, not significant as determined by student t test (E) Anti-fibronectin (green) staining
835 of fibroblast cells in the basolateral layer at 3h and 24h p.i. (F) Immunofluorescent microscopy
836 images of *C. difficile* infected IECs at 3h and 24h p.i. in the 3-D model. *C. difficile* filamentous
837 forms are observed at 24h p.i. (indicated by arrow). Inset below shows the orthogonal XZ axis
838 view of the IECs. *C. difficile* is stained green, actin, red and cell nuclei, blue, scale bar = 10 μM.
839
840 **Figure 7. *C. difficile* spores and toxin production, and host response to infection in the 3-D**
841 **model.** (A) Colony counts of spores and total cells in the host cell-associated *C. difficile* fraction
842 (infected cell lysates). Data shown is the mean of 3 independent experiments and error bars indicate
843 SD, ns, not significant as determined by two-way ANOVA. (B) Toxin A and B levels from apical
844 compartment supernatants as determined by ELISA in the 3-D model. Data shown is the mean of
845 3 independent experiments and error bars indicate SD, ns, not significant as determined by two-
846 way ANOVA. Grey line represents the sensitivity of the test at 0.5 ng/ml (C) Human IL-8 levels
847 in supernatants from the basolateral compartments with uninfected cells incubated for 24h or with
848 cells infected with *C. difficile* for 3h and 24h, as determined by ELISA. Grey line represents the
849 limit of detection at 32 pg/ml. Data shown is the mean of 3 independent experiments and error bars
850 indicate SD, $^{**}p < 0.01$. as determined by the one-way ANOVA.
851
852 **Figure S1. Characterization of mucus production in the Caco-2/HT29-MTX monolayer.**
853 Immunofluorescent microscopy images of Caco2/HT29-MTX monolayer (control, uninfected)
854 stained with mucin 2 antibody showing mucus production (green) after 14 days of cell culture in
855 the Snapwell insert. Actin is stained red and cell nuclei, blue. Scale bar = 10 μM.
856
857 **Figure S2. The vertical diffusion chamber maintains anaerobic conditions.** Overnight cultures
858 of *C. difficile* were centrifuged and equal numbers of bacteria (3.6 x 10^7 CFU/ml) were
859 resuspended in DMEM-10 and incubated in the VDC or anaerobic cabinet for 3h and 24h. Serial
860 dilutions of the apical supernatant were plated to enumerate colony counts. Data shown is the mean
861 of 3 independent experiments and error bars indicate SD, $p < 0.05$, ns, not significant by one-way
862 ANOVA).
863
864 **Figure S3: Change in TEER during *C. difficile* infection**
865 Reduction in TEER measurements at different times after infection. $^{*}p < 0.05$, $^{**}p < 0.01$ and
866 $^{***}p < 0.001$as determined by one-way ANOVA.
867
868 **Figure S4. Spore counts from apical chamber culture supernatants from monolayer model**
869 (A) Colony counts of spores and total cells in the apical compartment supernatants. A significant
870 decrease in total cell count was seen at 24h and 48h p.i. but an increase in spores compared to the

871 total bacterial numbers is observed. Data shown is the mean of 3 independent experiments and
872 error bars indicate SD, $p < 0.05$ as determined by two-way ANOVA.
873
874 **Figure S5. Fiber diameter of the electrospun nanofibrous matrix.** Fiber diameter analysis
875 revealed that the average fiber diameter was 457 ± 170 nm, with fibers in the range of 200-1100
876 nm (n=150 measurements, 50 measurements per scaffold from 3 independently produced
877 scaffolds).
878
879 **Figure S6. *C. difficile* spores and toxin production, and host response to infection in the**
880 **multilayer model.** (A) Colony counts of spores and total cells in the host cell-associated *C.*
881 *difficile* fraction of the multilayer model. Data shown is the mean of 3 independent experiments
882 and error bars indicate SD, ns, not significant as determined by two-way ANOVA. (B) Toxin A
883 and B levels in the multilayer model. Data shown is the mean of 3 independent experiments and
884 error bars indicate SD, ns, not significant as determined by two-way ANOVA. Dashed line
885 represents the sensitivity of the test at 0.5 ng/ml (C) Human IL-8 levels in the multilayer model.
886 Data shown is the mean of 3 independent experiments and error bars indicate SD, ns, not
887 significant as determined by the one-way ANOVA.
888
889 **Figure S7. Filaments are not produced when *C. difficile* is grown for 48h in culture in the**
890 **absence of intestinal epithelial cells.** (A). *C. difficile* was grown for 48 h using DMEM-10 and
891 stained with anti-*C. difficile* for 1h, followed by Alexa Fluor 488 goat anti-rabbit secondary
892 antibody (green). (B) The basolateral supernatant (DMEM-10) from a 24h infection in the VDC
893 was used to grow *C. difficile* for 48h to determine if cell released factors in the supernatant can
894 induce filament formation. Staining with anti *C. difficile* for 1h was performed, followed by Alexa
895 Fluor 488 goat anti-rabbit secondary antibody (green). Images were taken with a Leica DMi
896 microscope at 100x magnification. Scalebar =10 μM
897
898

Figure 1

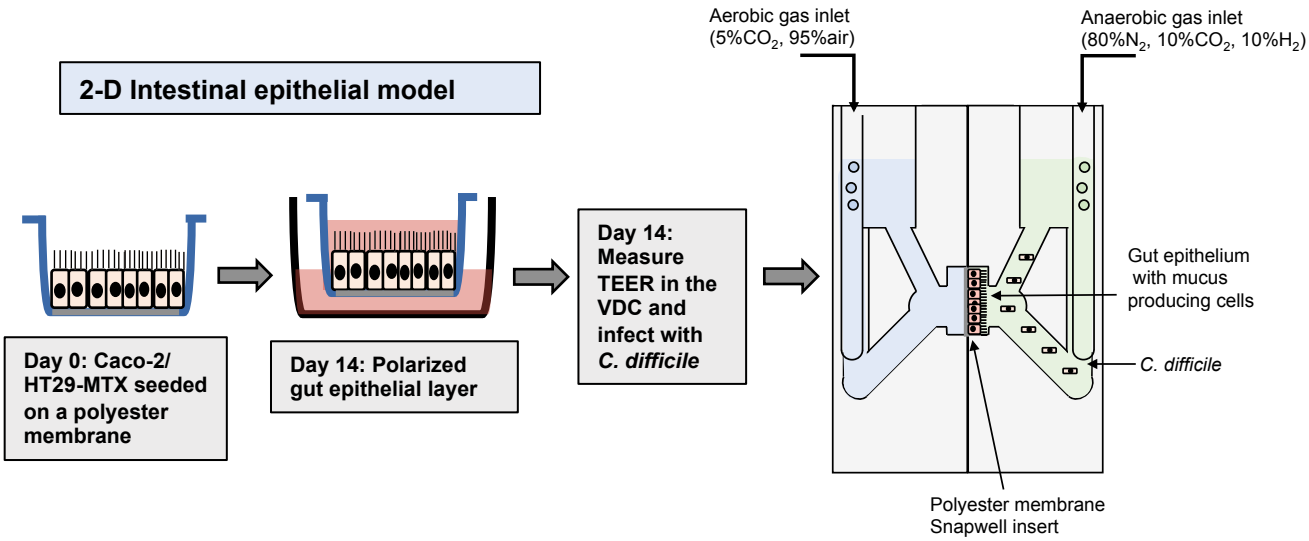
2-D Intestinal epithelial model
Day 0: Caco-2/ HT29-MTX seeded on a polyester membrane
Day 14: Polarized gut epithelial layer
Day 14: Measure TEER in the VDC and infect with C. difficile
Aerobic gas inlet (5%CO2, 95%air)
Anaerobic gas inlet (80%N2, 10%CO2, 10%H2)
Gut epithelium with mucus producing cells
C. difficile
Polyester membrane Snapwell insert

Figure 2

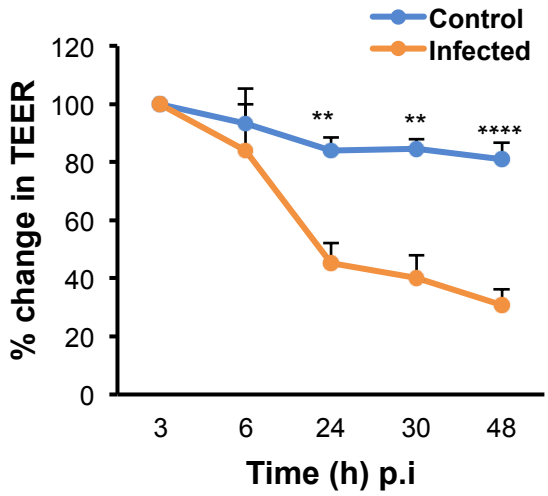
A
Control
Infected
% change in TEER
120
100
80
60
40
20
0
**
**
****
3
6
24
30
48
Time (h) p.i

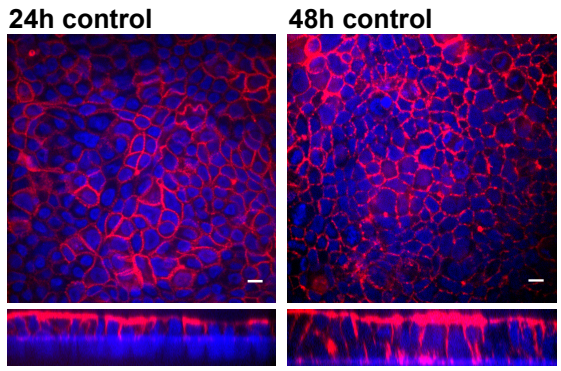
B
24h control
48h control

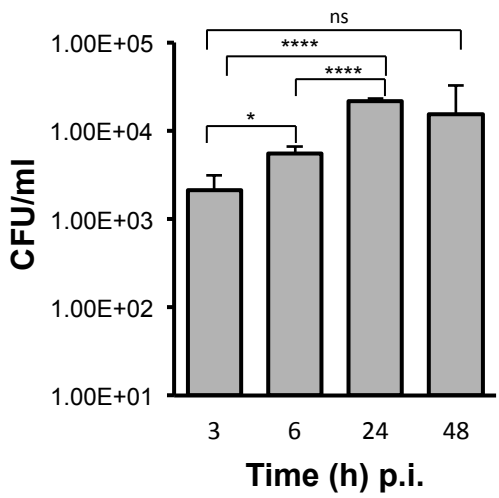
C
ns
****
****
*
CFU/ml
1.00E+05
1.00E+04
1.00E+03
1.00E+02
1.00E+01
3
6
24
48
Time (h) p.i.

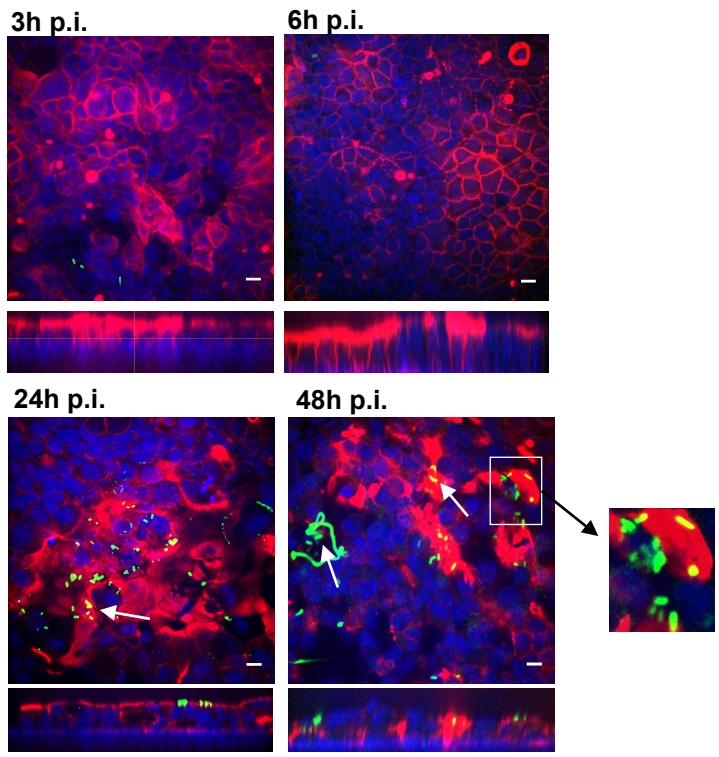
D
3h p.i.
6h p.i.
24h p.i.
48h p.i.

Figure 3

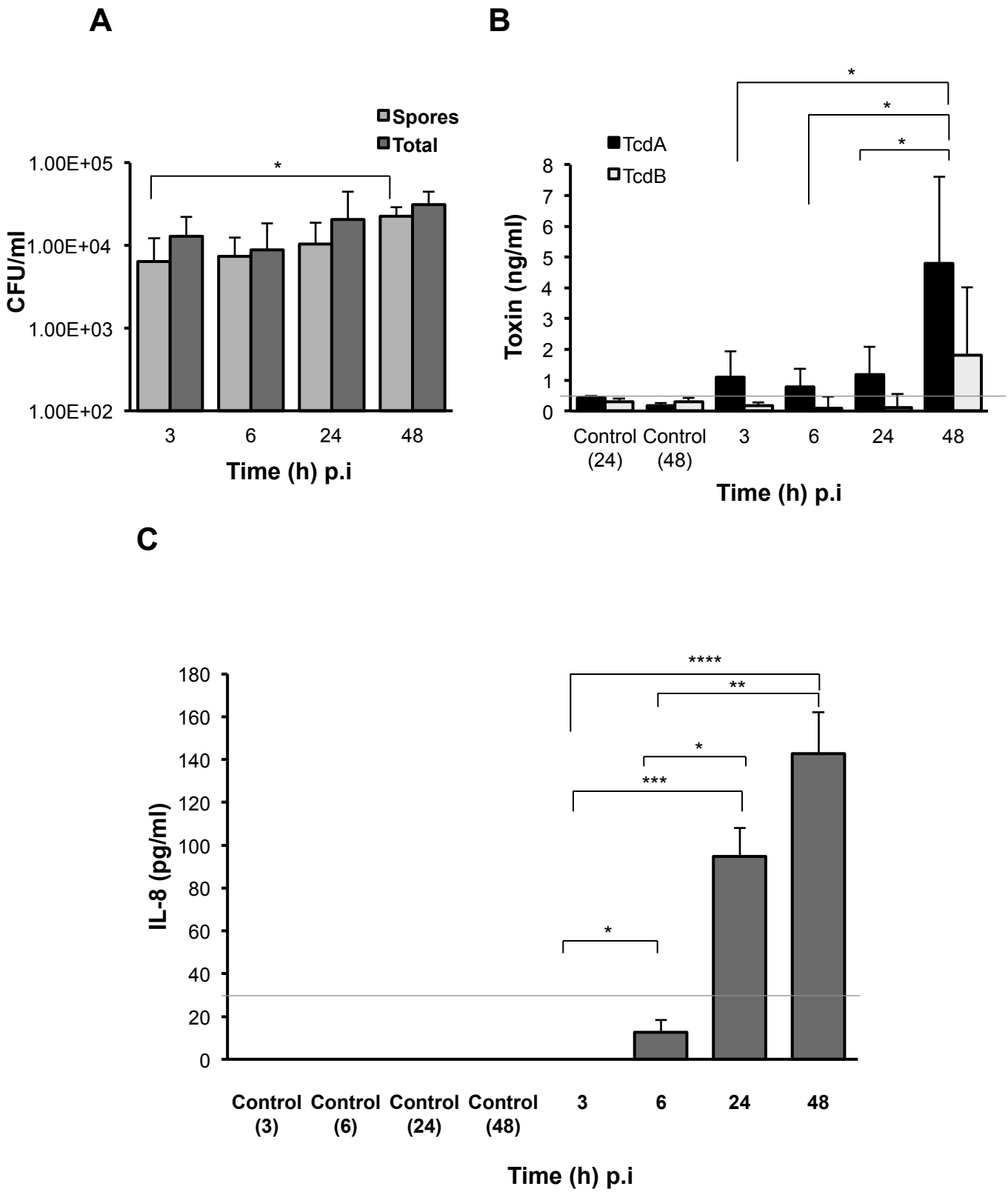
A
Spores
Total
1.00E+05
1.00E+04
1.00E+03
1.00E+02
CFU/ml
*
3
6
24
48
Time (h) p.i
B
TcdA
TcdB
Toxin (ng/ml)
0
1
2
3
4
5
6
7
8
*
*
*
Control (24)
Control (48)
3
6
24
48
Time (h) p.i
C
IL-8 (pg/ml)
0
20
40
60
80
100
120
140
160
180
****
**
*
***
*
Control (3)
Control (6)
Control (24)
Control (48)
3
6
24
48
Time (h) p.i

Figure 4

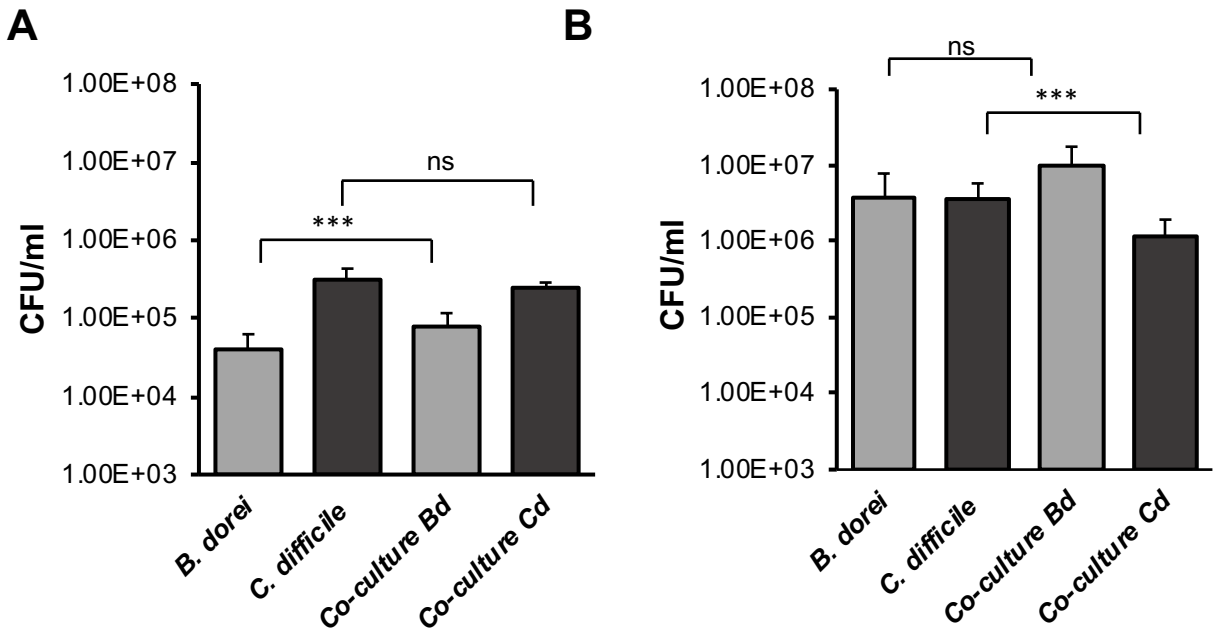
A
B
CFU/ml
1.00E+08
1.00E+07
1.00E+06
1.00E+05
1.00E+04
1.00E+03
***
ns
B. dorei
C. difficile
Co-culture Bd
Co-culture Cd

Figure 5

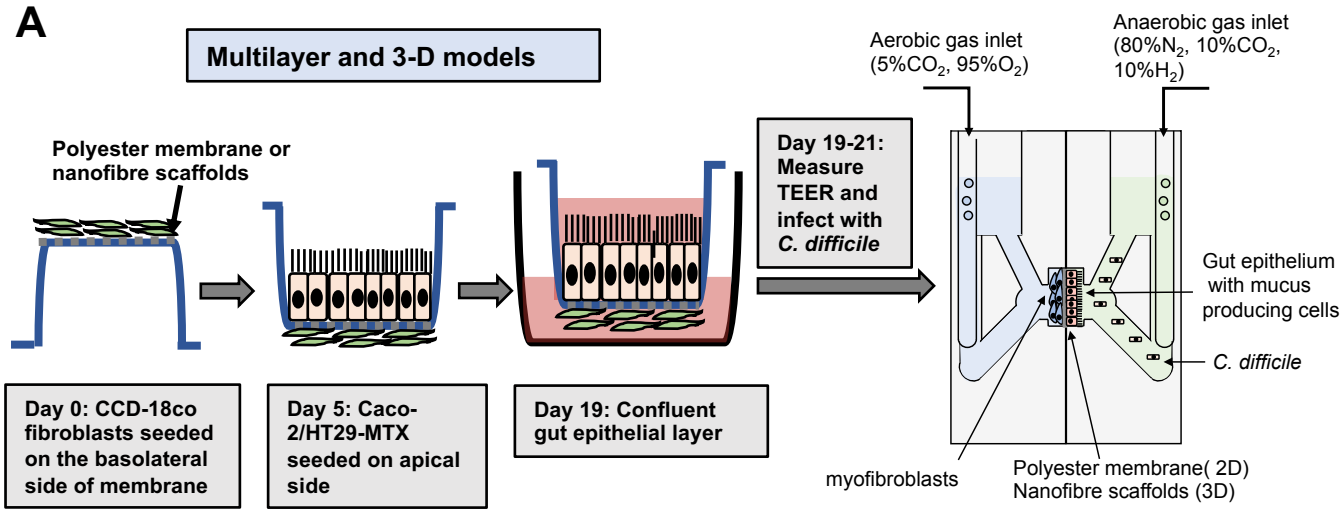
A
Multilayer and 3-D models
Polyester membrane or nanofibre scaffolds
Day 0: CCD-18co fibroblasts seeded on the basolateral side of membrane
Day 5: Caco-2/HT29-MTX seeded on apical side
Day 19: Confluent gut epithelial layer
Day 19-21: Measure TEER and infect with C. difficile
Aerobic gas inlet (5%CO2, 95%O2)
Anaerobic gas inlet (80%N2, 10%CO2, 10%H2)
Gut epithelium with mucus producing cells
C. difficile
myofibroblasts
Polyester membrane(2D)
Nanofibre scaffolds (3D)

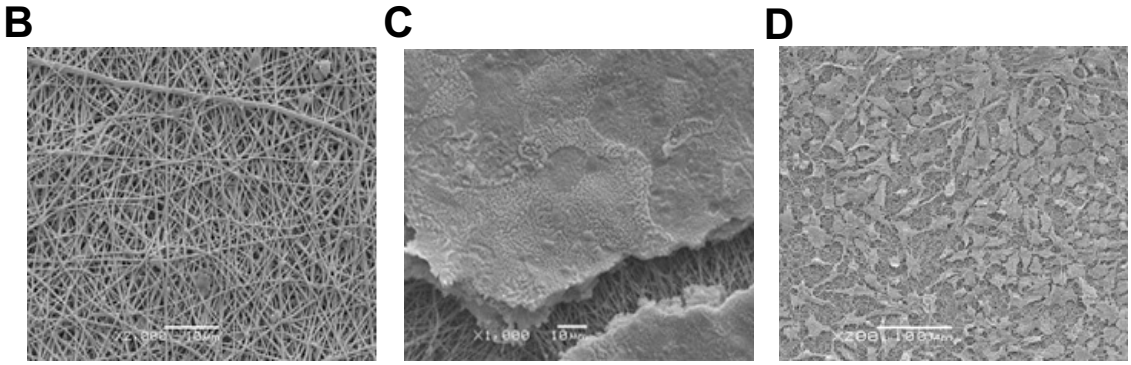
B
C
D

Figure 6

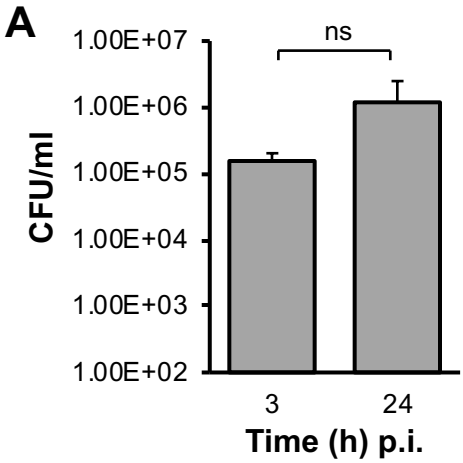
A
ns
1.00E+07
1.00E+06
1.00E+05
1.00E+04
1.00E+03
1.00E+02
CFU/ml
3
24
Time (h) p.i.

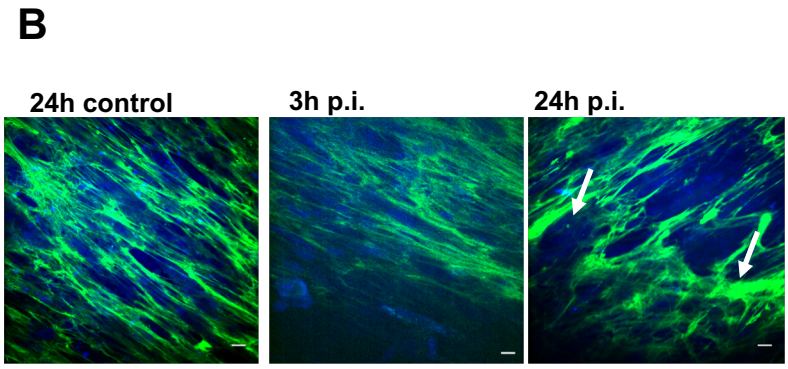
B
24h control
3h p.i.
24h p.i.

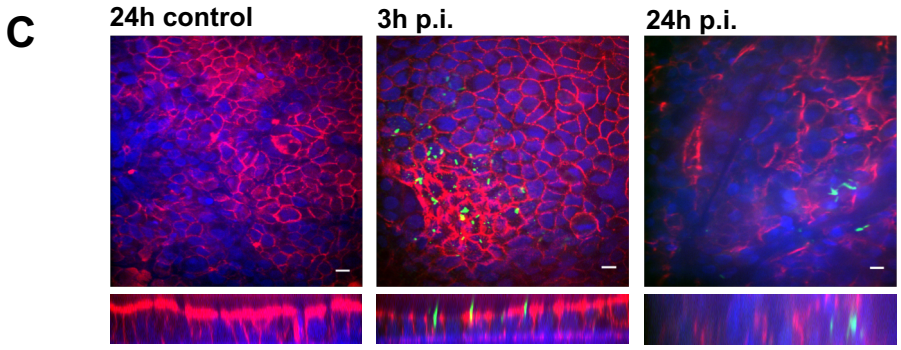
C
24h control
3h p.i.
24h p.i.

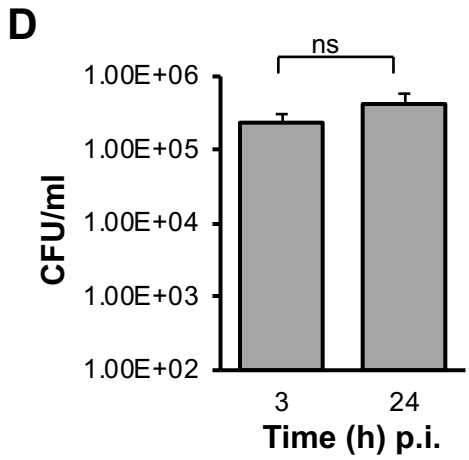
D
ns
1.00E+06
1.00E+05
1.00E+04
1.00E+03
1.00E+02
CFU/ml
3
24
Time (h) p.i.

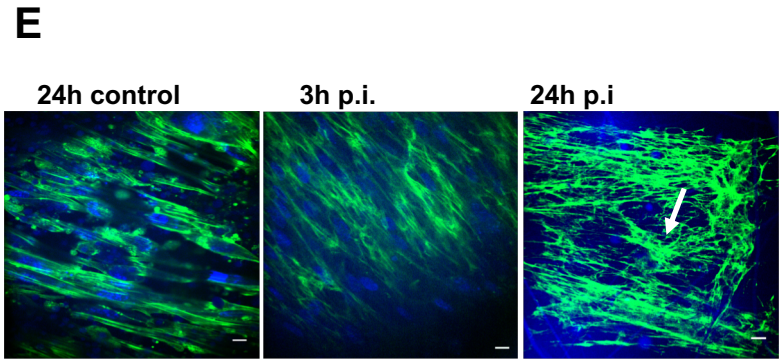
E
24h control
3h p.i.
24h p.i

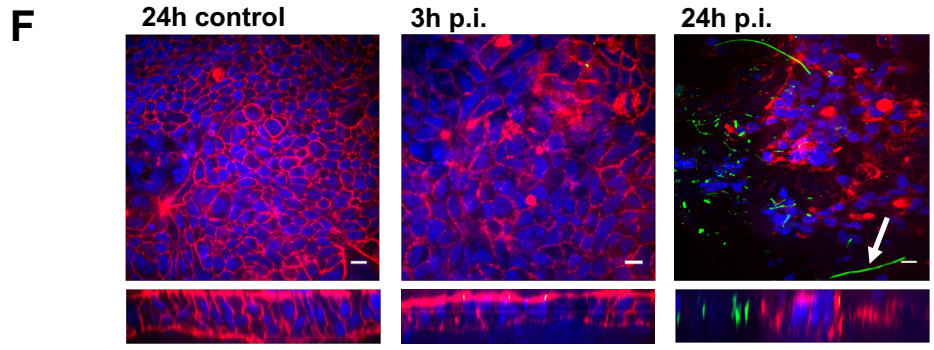
F
24h control
3h p.i.
24h p.i.

Figure 7

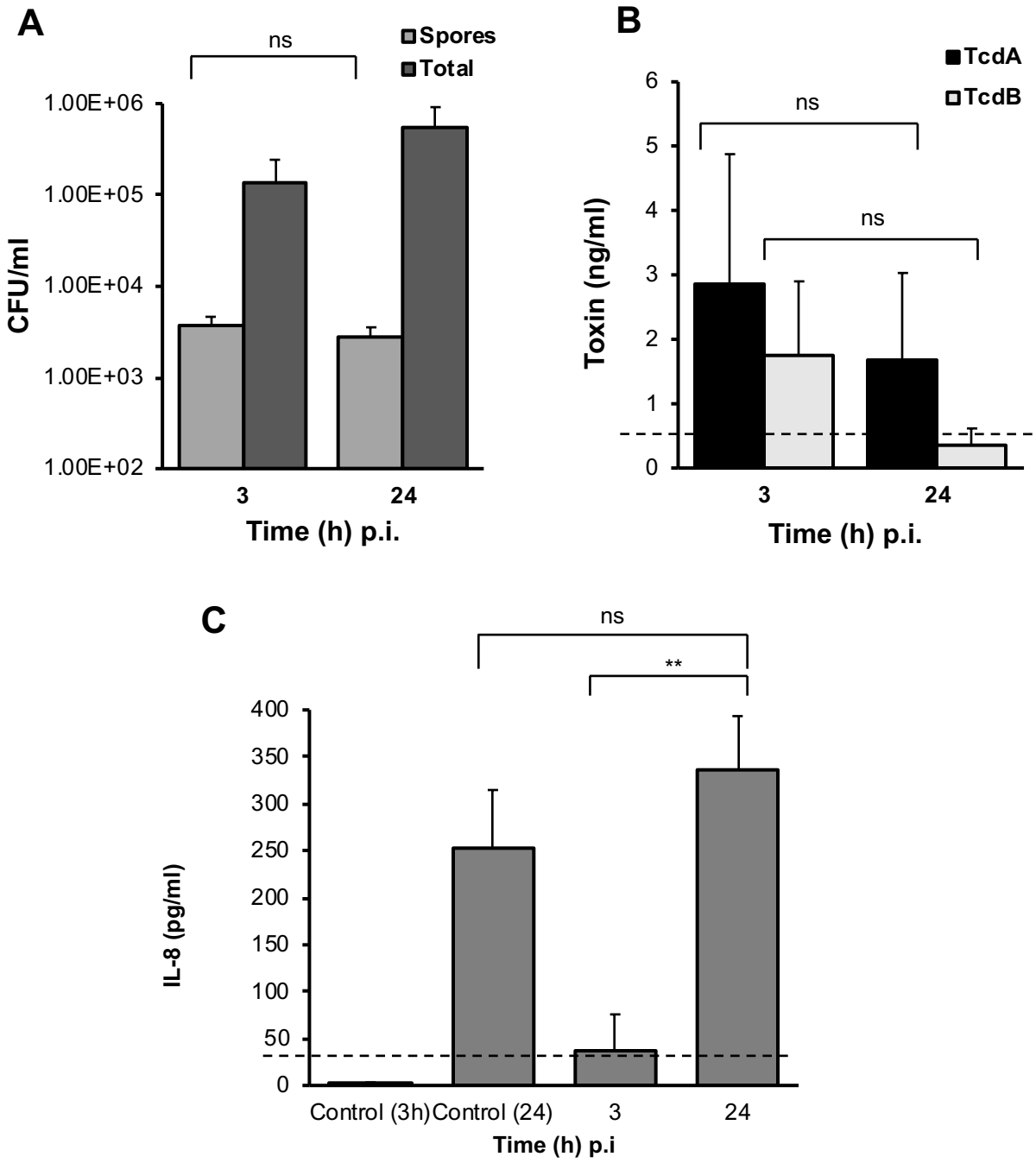
A
ns
Spores
Total
1.00E+06
1.00E+05
1.00E+04
1.00E+03
1.00E+02
CFU/ml
3
24
Time (h) p.i.
B
TcdA
TcdB
ns
ns
6
5
4
3
2
1
0
Toxin (ng/ml)
3
24
Time (h) p.i.
C
ns
**
400
350
300
250
200
150
100
50
0
IL-8 (pg/ml)
Control (3h)
Control (24)
3
24
Time (h) p.i

Table 1 Colocalisation analysis using ImageJ.Coloc 2.

	24h	**48h**
Li ICQ	0.135 +/- 0.0768	0.19 +/-0.0476
Manders tM1	0.16675 +/-0.1804	0.399 +/-0.0588
Manders tM2	0.3012 +/- 0.2089	0.2087 +/-0.1040
Costes P-value	1	1

Note: tM1 and tM2 represents the thresholded values for Manders' coefficient, M1 and M2. The maximum value that can be obtained for Manders and Costes is 1 and for Li ICQ, 0.5 (ICQ, intensity correlation coefficient).